ORIGINAL ARTICLE

Removal of paracetamol from aqueous solution with zinc oxide nanoparticles obtained by green synthesis from purple basil (*Ocimum basilicum* L.) waste

Alper Solmaz[1] · Talip Turna[2] · Ayşe Baran[3,4]

Abstract

In this study, environmentally friendly zinc oxide nanoparticles (OB-ZnO NPs) were synthesized using *Ocimum basilicum* (OB) plant waste extract, and the removal of paracetamol (PCM) from pharmaceutical wastes with toxic effects on the ecosystem was investigated. The characteristic structure of synthesized OB-ZnO NPs was determined by X-ray diffraction (XRD), Brunauer–Emmett–Teller (BET), scanning electron microscope (SEM) and energy dispersive X-ray (EDX), Fourier transform infrared spectroscopy (FT-IR), dynamic light scattering (DLS), Zetasizer, thermogravimetry-differential thermal analysis (TGA-DTA), and UV-vis spectroscopy. The effect of the obtained OB-ZnO NPs on PCM removal was determined by batch adsorption tests. In the study in which 6 different kinetic and isotherm models were examined, error analysis functions were used to determine the most suitable model. Accordingly, the crystal structure of biosynthesized OB-ZnO NPs has a particle size of 30.39 nm, a surface area of 13.826 m^2/g, and a pore volume of 0.0475 cm^3/g. Since OB-ZnO NPs have a zeta potential of -22.1 mV and a mass loss of 33% at about 750 °C, these NPs show that they are durable at high temperatures. When the PCM removal mechanisms with OB-ZnO NPs were examined, it was determined that the most suitable kinetic and isotherm model was the Elovich model with an R^2 value of 0.989 and the Redlich-Peterson model with an R^2 value of 0.999. In the study, which reached 23 mgPCM/gOB-ZnO NP removal efficiency, it was revealed that OB-ZnO NPs obtained from waste plants have the potential to be used in the removal of pharmaceutical wastes.

Keywords Green synthesis · *Ocimum basilicum* · Nanoparticle · Paracetamol · Adsorption · Wastewater treatment

✉ Alper Solmaz
alper.solmaz@iste.edu.tr

Talip Turna
talipturna@gmail.com

Ayşe Baran
ayse.gorgec43@gmail.com

1   Department of Environmental Protection and Control-Iskenderun Vocational School of Higher Education, Iskenderun Technical University, Hatay, Turkey

2   Department of Parks and Garden Plants-Diyarbakır Vocational School of Higher Education, Dicle University, Diyarbakır, Turkey

3   Batman University Food Analysis Application and Research Center, Batman University, Batman, Turkey

4   Faculty of Health Sciences, Malatya Turgut Özal University, Malatya, Turkey

1 Introduction

Clean water is needed for all components of the ecosystem to be healthy and happy. In most countries, the lack of clean water has become a critical problem [1]. Discomforts caused by this critical problem are making the use of pharmaceutical products more and more widespread. From pharmaceutical products, analgesic and antipyretic drugs are among the most used drugs worldwide. Acetaminophen, or PCM, is currently one of the most widely used analgesic and antipyretic drugs available over the counter worldwide [2, 3]. Less than 15% of PCM is absorbed by the patient's body; the rest is excreted in the urine and reaches the sewer system [4]. Acetaminophen or PCM is increasingly found in the natural aquatic environment today due to its wide use and consumption. Moreover, it has been frequently detected in water, sediment, sewage sludge, and soil [5]. It has also been reported that it is widely detected in natural waters and drinking waters [6].

PCM is in a convertible form to various intermediates depending on environmental conditions, although its concentrations are usually in the ppt to ppm range [4].

Since PCM is widely excreted into the aquatic environment, it can cause hepatotoxicity and nephrotoxicity in aquatic organisms, resulting in death in aquatic ecosystems or adversely affecting the next consumer level. PCM also has toxic effects on plants. For example, in a study with *Triticum aestivum* L. (wheat), the shoot and root elongation of the plant was slowed after chronic exposure to PCM [7]. In the exposure study performed on *Rhamdia quelen* male fish, it was stated that PCM disrupted the hypothalamic-pituitary-gonadal axis in *Rhamdia quelen*, caused changes in hematological parameters, and caused hepatotoxicity. PCM is also prone to bioaccumulation in aquatic organisms [8]. PCM is frequently found in significant quantities in wastewater discharges and thus in the aquatic environment, raising ecotoxicity concerns, particularly for aquatic non-target species [9]. In a study on the exposure of sea snail *Gibbula umbilicalis*, it was stated that this species was prooxidatively affected by PCM [10].

PCM has also been widely detected in the aquatic ecosystem. A total of 30.421 ng/L PCM was detected in a 3-year study in the Monjolinho river in São Paulo, Brazil [11]. In a study conducted in seawater, it was reported that the PCM level in seawater in the north of Portugal (Vila do Conde) increased up to 76.9 ng/L [12]. Again, in another study conducted in Sydney estuary, it was reported that one of the 8 pharmaceuticals detected was PCM [13]. In the study conducted in Peru by identifying 38 target pharmaceuticals in surface and well waters, it was reported that PCT was the drug with the highest concentration (> 100 μg/L) [14].

In the literature, micropollutants such as nonsteroidal anti-inflammatory drugs, antidepressants, and antibiotics have been removed by various methods [15]. Some of these are processes such as chemical oxidation processes (such as electrochemical, ozone, Fenton, and UV/H$_2$O$_2$), which are mainly carried out by the oxidizing activity of hydroxyl radicals [16, 17], biological processes (classical activated sludge process, heterotrophic, and autotrophic mixed culture) which generally occur with evaporation, metabolic utilization and biodegradation [18], ultrasonic degradation mainly due to the occurrence with free radicals produced at different temperatures [19], and membrane filtration processes which are carried out by size difference and electrostatic charge repulsion [20, 21]. Although these technologies have many advantages in their own fields, they have some disadvantages in terms of investment and operating costs, process complexity, and process controllability [22]. In recent years, the adsorption method (activated carbon, biochar, biosorbent, and nanoparticles) which is based on the mechanism of physical/chemical adhesion to the surface has become one

of the preferred methods due to its cheap production and relatively easy and flexible operation. [23].

Recently, the necessity of making biocompatible materials for applications in different fields such as health, medicine, water treatment, and purification has led to more interest in the field of nanotechnology [24]. Adsorption principle and nanotechnological materials are among the most widely used technologies in removing pollutants from water. Traditional methods have been used in the production of nanoparticles for a long time, but research has proven that green methods are more advantageous in the production of NPs due to their positive aspects such as less chance of failure, low cost, and ease of characterization [25]. Green synthesis methods are attracting the attention of researchers because of their potential to reduce the toxicity of NPs. Therefore, the use of vitamins, amino acids, fungi, enzymes, actinomycetes, bacteria, algae, yeasts, and plant extracts in green synthesis methods has become a very popular topic today [26]. In addition, there is an intense interest in the biosynthesis of metal nanoparticles derived from organisms. Among these organisms, plants appear to be the best candidates and are suitable for large-scale biosynthesis-production of nanoparticles. Nanoparticles produced by plants are more stable and more diverse in shape and size than those produced by other organisms [27, 28]. The development of metallic nanoparticles using biological materials with an environmentally friendly approach has received great attention. Recently, nano-sized metals such as Fe$_3$O$_4$, TiO$_2$, MgO, CuO, and ZnO have been used in biological applications by researchers [29]. Among the semiconductor metal NPs, ZnO is used in many wastewater treatment applications due to its environmentally friendly nature [30, 31]. ZnO directly provides a wide band gap (3.37 eV) and photocatalytic activity to remove toxic chemicals from the environment [32]. The exciton binding energy (60 meV) of ZnO at room temperature has a wide range of applications in solar cells, optics and electricity, gas and chemical sensing, biomedical applications, and catalysis and photocatalysis [31, 33].

There are few studies in the literature on nanoparticle production from the OB plant. In these studies, coatings were made with metals such as silver, Au-Ag, and TiO2. However, in this and similar studies, characterization studies of the produced material were generally carried out, and some researchers focused on the antimicrobial efficiency of the produced product. However, no research has been found on the removal of any pollutants with these NPs [34–36].

In this study, it was aimed to remove paracetamol from pharmaceutical wastes from aquatic environment with OB-ZnO NPs synthesized by the green synthesis method from wastes of the OB plant. Characterization studies (XRD, BET, SEM-EDX, FTIR, DLS, Zetasizer, TGA-DTA, and UV-vis) of synthesized OB-ZnO NPs were performed. In adsorption studies with OB-ZnO NPs, 6 different isotherm and kinetic models
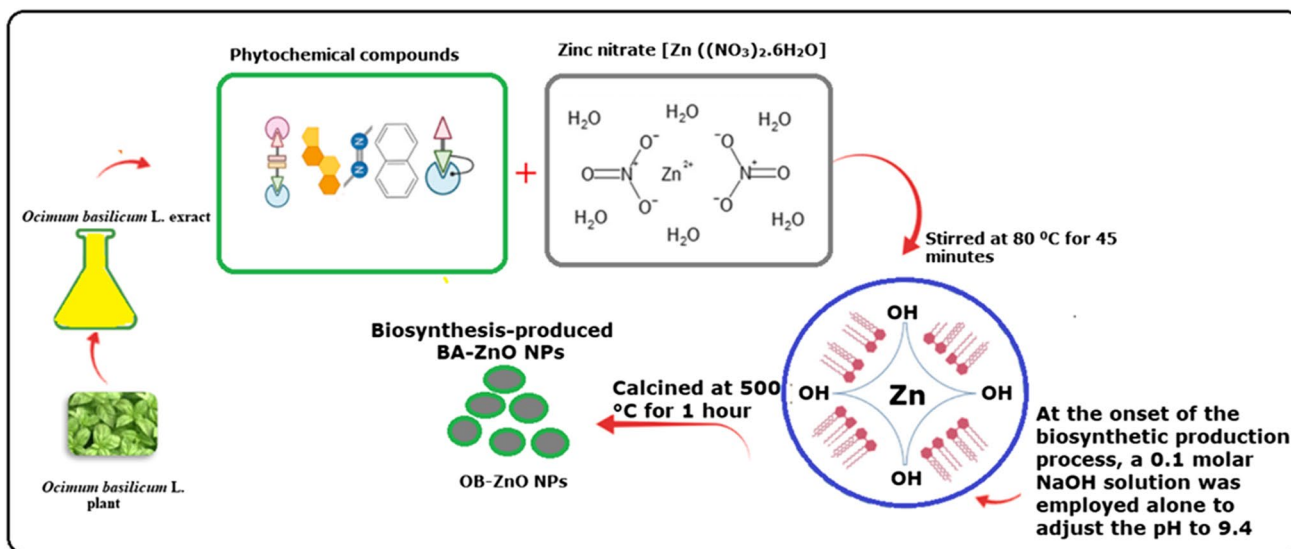
Fig. 1 Schematic of the production of OB-ZnO NPs using phytochemicals extracted from OB

were tested, and the most appropriate isotherm and kinetic model was determined by using error sum of squares (SSE), sum of absolute errors (SAE), average relative errors (ARE), hybrid fractional error function (HYBRID), Marquardt's percent standard deviation (MPSD), and non-linear chi-square test (X^2) error functions to determine the most suitable model.

Table 1 Kinetic and isotherms model used in adsorption studies

|	Model	Reaction equation	Definitions of terms	References
Kinetics models	Pseudo-first-order	$\frac{dq_t}{d_t} = K_1(q_{e-}q_t)$	q_e and q_t denote the amount of PCM (mg/L) at any time t in equilibrium K_1 pseudo first order reaction constant (1/min)	[42]
	Pseudo-second-order	$\frac{dq_t}{d_t} = K_2(q_{e-}q_t)^2$	K_2 pseudo second order reaction constant (1/min)	[43]
	Elovich	$q_t = \frac{1}{\beta}\ln(\alpha\beta) + \frac{1}{\beta}\ln t$	α is the initial adsorption rate (mg/g) β is the desorption constant (g/mg)	[44]
	Intra-particle diffusion	$q_t = K_{id}t^{1/2} + C$	K_{id} is the model constant. K_{id} is obtained by plotting the value of $t^{1/2}$ against the value of q_t in the equation	[45]
	Liquid film diffusion	$\ln(1 - F) = -k_{fd}t$	k_{fd} is the model constant	[45]
	Bangham	$q_t = q_e(1 - e^{k_b t^2}$	k_b is the model constant	[46]
Isotherms model	Freundlich	$q_e = K_F C_e^{1/n}$	q_e is the the amount of pollutant adsorbed at equilibrium (mg/g) K_F and n are model constants C_e is the amount of pollutant remaining in equilibrium	[47, 48]
	Langmuir	$q_e = \frac{q_{max}K_L C_e}{1+K_L C_e}$ $R_L = \frac{1}{1+a_L C_e}$	R_L is dispersion constant K_L is Langmuir adsorption constant a_L Langmuir constant	[48, 49]
	Temkin	$q_e = B\ln(A_T C_e)$ $B = \frac{RT}{b_T}$	B is the cautious constant (J/mol) R is the universal gas constant (8.314 j/mol.K) T is temperature (K) b_T is the heat of isotherm constant (kj/mol),	[50, 51]
	Dubinin–Redushkevich	$q_e = q_m\exp(-Be^2)$ $e = RT\ln(1 + \frac{1}{C_e})$	e is the Polanyi potential	[52]
	Redlich-Peterson	$q_e = \frac{K_R C_e}{1+\alpha C_e^\beta}$	K_R are Redlich–Peterson model constants β is the exponent of model	[53]
	Sips	$q_e = \frac{K_S C_e^\beta S}{1+a_S C_e^\beta S}$	a_S Sips isotherm model constant	[54]

Table 2 Error functions and definitions used

Error function	Equation	Description	References
Error sum of squares (SSE)	$SSE = \sum (q_{e,cal} - q_{e,exp})^2$	It is an expression of diversity in the cluster	[55]
Sum of absolute errors (SAE)	$SAE = \sum_{i=1}^{n} \left\| q_{e,exp} - q_{e,cal} \right\|$	It is the sum of the absolute errors between the experimental results and the calculated values	[51]
Average relative errors (ARE)	$MRAE = \frac{1}{n} \sum_{i=1}^{n} \left\| \frac{q_{e,cal} - q_{e,exp}}{q_{e,exp}} \right\|$	It is the ratio of the sum of the absolute errors between the experimental results and the calculated values to the experimental result	[56, 57]
Hybrid fractional error function (HYBRID)	$MRAE = \frac{1}{N-P} \sum \left\| \frac{q_{e,exp} - q_{e,cal}}{q_{e,exp}} \right\|$	It is the SSE values divided by the estimated value	[55]
Marquardt's percent standard deviation (MPSD)	$MRAE = \sqrt{\frac{\sum \left\| (q_{e,exp} - q_{e,cal})/q_{e,exp} \right\|^2}{N-P}}$	It is a model similar to the geometric error distribution	[58]
Non-linear chi-square test (X^2)	$X^2 = \sum \frac{(q_{e,exp} - q_{e,cal})^2}{q_{e,cal}}$	It is the ratio of the square of the difference between the experimental results and the calculated values to the calculated values	[55]

2 Material and method

2.1 Chemicals

The chemicals used in experimental studies were of analytical purity, and distilled water was used in the preparation of all solutions. Powder paracetamol (C_8H_9NO, 151.16 g/mol, 98.0%, Sigma-Aldrich), pellet sodium hydroxide (NaOH, 40.00 g/mol, $\geq 99.0\%$, Sigma-Aldrich), liquid sulfuric acid ($H_2(SO_4)_3$, 98.08 g/mol, $\geq 99.99\%$, Merck), powder zinc oxide (ZnO, 81.39 g/mol, $\geq 99.0\%$, Merck) and zinc nitrate hexahydrate ($Zn(NO_3)_2.6H_2O$, 327 g/mol, 98%, Sigma-Aldrich), and liquid hydrochloric acid (HCl, 36.6 g/mol 1.19 g/cm^3, 37%, Sigma-Aldrich) were used. 0.1 M NaOH and 0.1 M H_2SO_4 were used for pH adjustment.
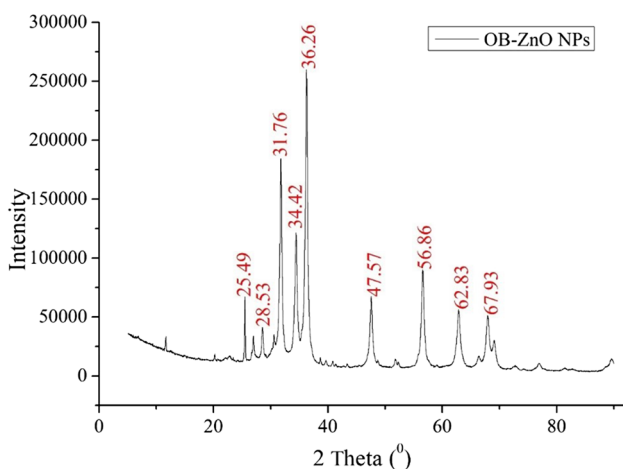
Fig. 2 XRD diagram of OB-ZnO NPs obtained with basil stalks

2.2 Preparation of extract of OB plant stems

OB plant was collected in the Mazıdağı district of Mardin (Turkey) province in July. The OB handles were thoroughly rinsed with tap water to remove dust particles and then washed again with distilled water. It was dried in the shade for about 5 days, and the stem parts of the plant used in the experimental studies were pulverized. Thirty grams of plant stem powder was mixed with 200 mL of distilled water and heated at 85 °C for 60 min. The solution was cooled then filtered using Whatman filter paper, and the resulting stem extract was stored at 4 °C.

2.3 Biosynthesis of OB-ZnO NPs

For nanoparticle synthesis, 300 mL of a 0.1-M solution of zinc nitrate salt was added to a reaction vessel. Then, 100 mL of the stalk extract of the OB plant, which was prepared before, was added. Then the mixture was left in the reaction medium at 80 °C for 45 min. Phytochemicals, which consist of bioactive groups including hydroxyl and amine groups, are present in plant extracts. These phytochemicals participate in redox processes and work as a reducing and stabilizing force to convert the ionized Zn^{+2} valence form to the ZnO state [37, 38]. Consequently, the production and stability of BA-ZnO NPs

Table 3 BET analysis of the OB-ZnO NPs

Parameter	Result
Surface area (m^2/g)	13.826
BJH* total pore volume (cm^3/g)	0.0475 cm^3/g
BJH average pore diameter (nm)	30.39 nm
Isotherm type	Adsorption
Average particle radius (nm)	6.88

*BJH, Barrett-Joyner-Halenda

Fig. 3 N$_2$ adsorption isotherms of OB-ZnO NPs
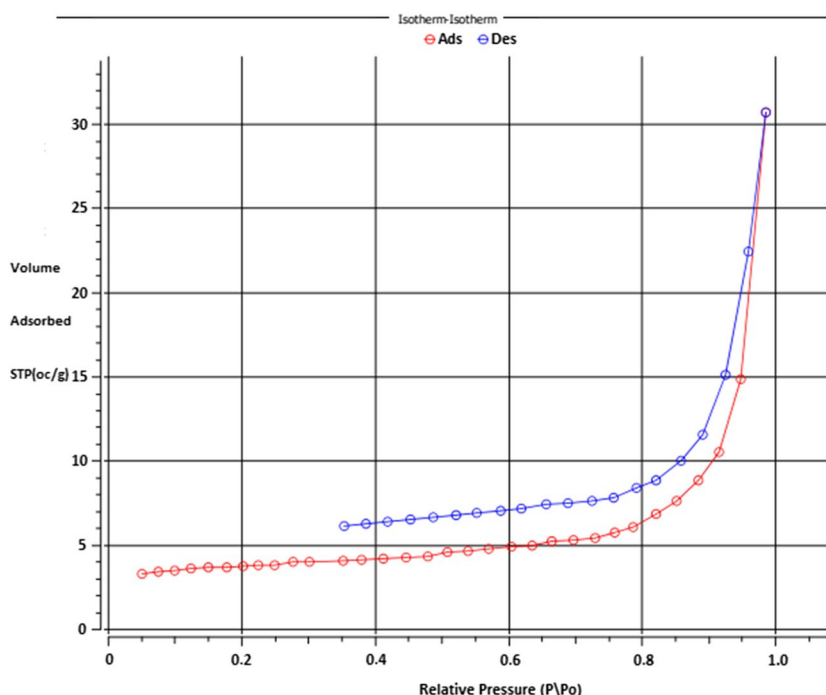
can be attributed to the phytochemicals present in the plant extract. At the onset of the biosynthetic production process, a 0.1-molar NaOH solution was employed alone to adjust the pH to 9.4 [39–41]. Biosynthesis was thereafter commenced, and 45 min passed following the production of BA-ZnO NPs in the initial 15 min (Fig. 1).

The reaction was terminated when the color of the solution changed to light brown. The resulting solution was centrifuged at 4500 rpm. The solid was washed five times with distilled water. Then, the solid part was left on a glass pellet, dried in an oven at 65 °C and calcined at 500 °C for 1 h. The obtained biologically sourced OB-ZnO NPs were stored for use in the absorption process.

2.4 Adsorption studies

Experimental analysis was carried out in three repetitions. In order to determine the optimum pH, experiments were carried out at pH 3,5,7,9, and 11 in the presence of 0.005 g adsorbent in a volume of 10 mL in the presence of an initial concentration of 100 mg/L PCM. Then, isotherm studies were carried out in the presence of 0.0125 g adsorbent at 0–200 mg/L PCM concentrations in a volume of 25 mL at room temperature, pH 6, for 24 h. For the kinetic study, removal efficiencies were investigated at a PCM concentration of 100 mg/L in the presence of 0.1 g adsorbent in 50 mL volume at pH 6 at room temperature. The PCM concentration in each solution was measured at a wavelength of 242 nm in a UV–vis spectrophotometer (Hach DR6000)

by passing through a 0.45 membrane filter attached to the syringe tip. In the interpretation of the results, the removal efficiency (R) was calculated using Eq. 1, and the calculation of the amount of PCM removed per unit adsorbent (q_e) was calculated using Eq. 2.

$$R(\%) = \left(\frac{C_0 - C_e}{C_0} \right) \times 100 \qquad (1)$$

In Eq. 1, C_0 and C_e represent the initial and equilibrium concentration (mg/L) of PCM, respectively.

$$q_e = \frac{(C_0 - C_e) \times V}{m} \qquad (2)$$

In Eq. 2, again, C_0 and C_e represent the initial and equilibrium concentration of PCM, respectively (mg/L), m represents the amount of adsorbent used (g), and V represents the total volume of the solution (L).

2.5 Adsorption kinetics and isotherms

Six different kinetic and six different isotherm models were used to interpret the studies. The equations of the models used and the definitions of the real terms in these equations are presented in Table 1.

2.6 Error function test describing

Various error functions that try to interpret the values and explain the relationship between these values by analyzing

Fig. 4 SEM images of OB-ZnO NPs before reaction, **a** 1 µm (Mag, 10 KX), **b** 200 nm (Mag, 20 KX), **c** 100 nm (Mag, 30 KX), **d** 100 nm (Mag, 50 KX), **e** 5 µm full area, **f** elemental compositions, and **g** EDX graph showing percentage (%)
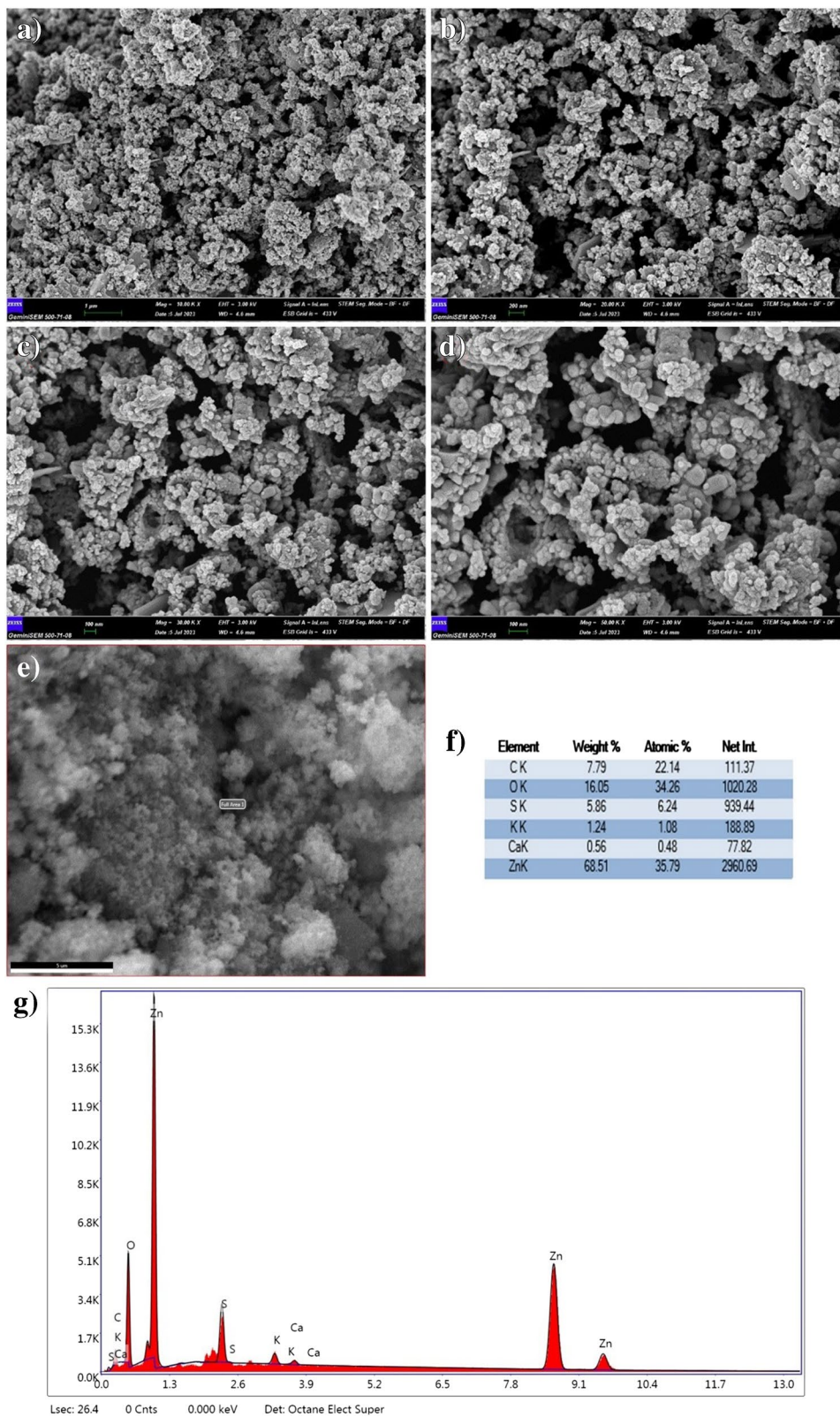
Table 4 Kinetic parameters calculated for the sorption of MB onto OB-ZnO NPs

Kinetic models	Pseudo first order	Pseudo second order	Elovich	Intra-Particle Diffusion	Liquid film diffusion	Bangham
Parameters	$k_1 = 0.052$	$k_2 = 7113$	$\beta = 907.353$	$ki = 0$	$k_{fd} = 0.037$	$m = 3.82$
		$q_e = 0.008$	$\alpha = 0.003$	$a = 0.002$		$k_r = 0.002$
R^2	0.873	0.982	0.989	0.771	0.885	0.929
SSE	0.000	0.000	0.000	0.000	0.000	0.000
SAE	0.016	0.004	0.003	0.003	0.002	0.005
ARE	65.31	19.19	4.22	17.47	24.91	11.17
HYBRID	92.435	16.898	0.920	10.309	95.213	6.719
MPSD	0.999	0.982	0.954	0.978	0.990	0.9703
X^2	0.012	0.001	0.000	0.001	0.000	0.000

R^2 coefficient of determination, *SSE* sum of squares errors, *SAE* sum of absolute errors, *ARE* average relative errors, *HYBRID* hybrid fractional error function, *MPSD* Marquardt's percent standard deviation, X^2 non-linear chi-square test

the results obtained from the experimental studies were used. These error functions are summarized in Table 2 [51].

3 Results and discussion

3.1 Characterization of OB-ZnO NPs of biogenic origin

OB-ZnO NPs obtained from basil stalks were characterized using different techniques. The optical absorption spectrum was first determined with a UV-vis spectrophotometer (UV-1800, SHIMADZU, Kyoto, Japan) at the maximum formation wavelength of OB-ZnO NPs in the 250–800 nm range. Functional groups of synthesized OB-ZnO NPs before and after absorption were determined by Fourier transform infrared spectrometer (SHIMADZU) binding. The morphological structure of OB-ZnO NPs before and after absorption was determined by energy-dependent field emission scanning electron microscopy SEM-EDX (JEOL, Tokyo, Japan) at different magnification scales. Electron-dispersed X-rays of nanoparticles were used to indicate the elemental composition in the structure. The crystal size of nanoparticles was determined by using the X-ray diffraction analysis method (XRD) in the range of OB-ZnO NPs 2θ: 2–80. For particle size distribution and zeta potential, OB-ZnO NPs were sonicated for 5 min for samples and then quantified with Malvern Zetasizer (Malvern Instruments Ltd., Malvern, UK).

3.2 X-ray diffraction (XRD)

X-ray diffraction was used to examine the manufactured material's crystal structure. A system for X-ray diffraction with a range of 1 to 80 A was used to find the X-ray diffraction pattern of OB-ZnO NPs. Figure 2 shows the XRD structures of green synthesized OB-ZnO NPs. Powdered OB-ZnO NPs exhibited a series of peaks at 2θ and 31.76°, 34.42°, 36.26°, 47.57°, 56.86°, 62.83°, 67.93°, 72.00°, and 76.00° on the X-ray diffraction pattern. The peaks seen correspond to the expansion of the lattice planes associated

Table 5 Calculated isotherm parameters for the sorption of PCM onto OB-ZnO NPs

Isotherms	Freundlich	Langmuir	Temkin	Dubinin-Radushkevich	Redlich-Peterson	Sips
Parameters	$k_F = 0.055$	$k_L = -0.112$	$B_T = -522.58$	$k_D = -5.757$	$\alpha = 1.155$	$n = -0.681$
	$1/n = -0.153$	$R_L = 1.003$	$k_T = 0$	$q_s = 0.029$	$a_R = 15.715$	$k_s = 0.004$
		$q_{max} = 0.023$			$k_R = 0.878$	
R^2	0.921	0.993	0.943	0.284	0.999	0.999
SSE	0.000	0.017	0.000	0.000	0.000	0.005
SAE	0.006	0.137	0.005	0.015	0.006	0.157
ARE	3.7	75.5	2.8	10.1	3.7	100.0
HYBRID	0.13	114.29	0.24	1.16	0.18	249.99
MPSD	0.936	1.001	0.942	0.956	0.939	1.009
X^2	0.000	0.450	0.000	0.002	0.000	0.157

Fig. 5 SEM images of OB-ZnO NPs after reaction, **a** 1 μm (Mag, 10 KX), **b** 200 nm (Mag, 20 KX), **c** 100 nm (Mag, 30 KX), **d** 100 nm (Mag, 50 KX), **e** 5 μm full area, **f** elemental compositions, and **g** EDX graph showing percentage (%)
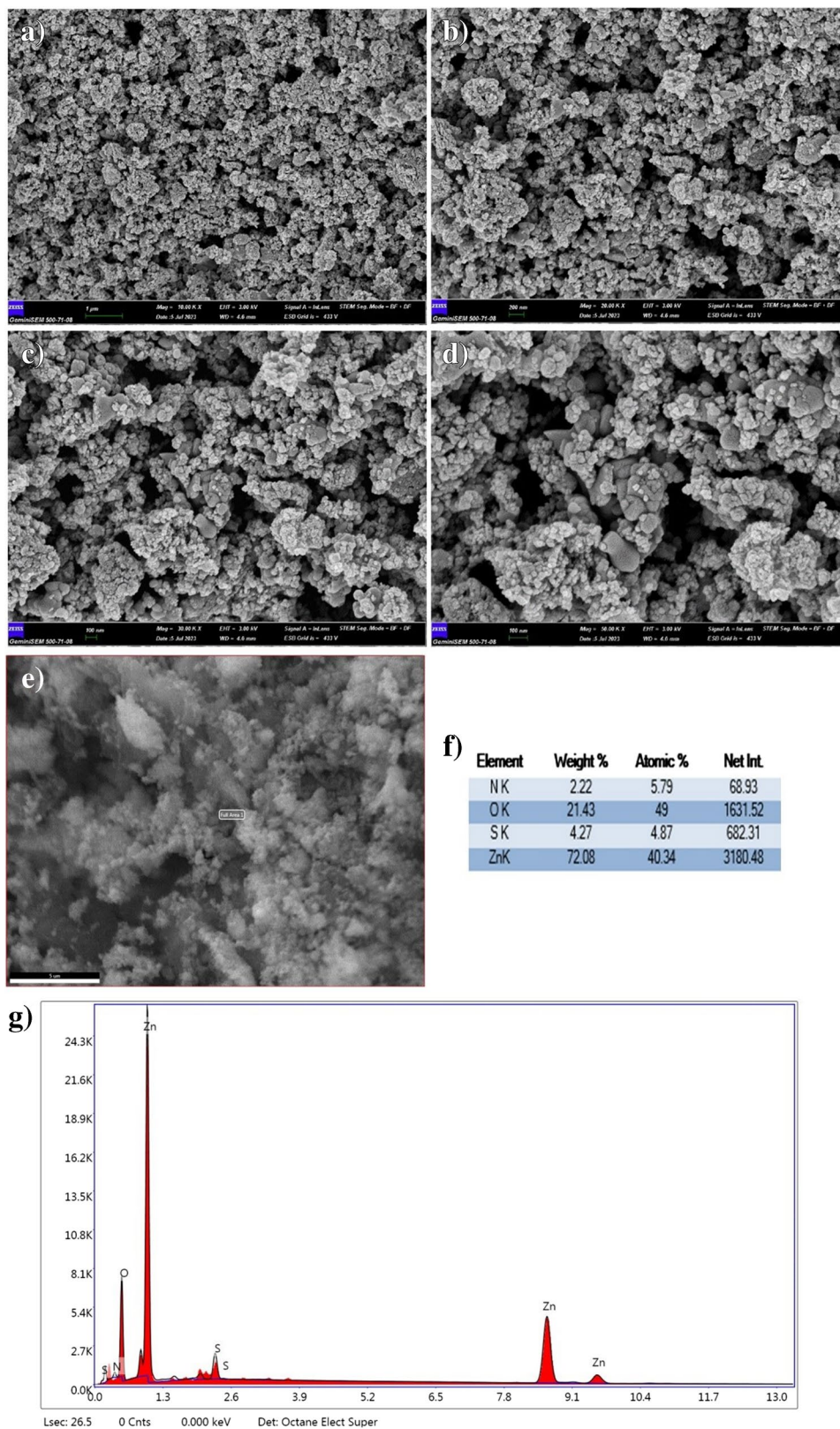
with Bragg's angles (100), (002), (101), (102), (110), (103), (200), (112), (004), and (202). BA-ZnO illustrates the crystal structural pattern of NPs. The parallelism of the crystal pattern (hexagonal wurtzite structure) of BA-ZnO NPs as determined by XRD is consistent with the JCPDS no.: 36–1451 standard powder diffraction model [40, 41, 59].
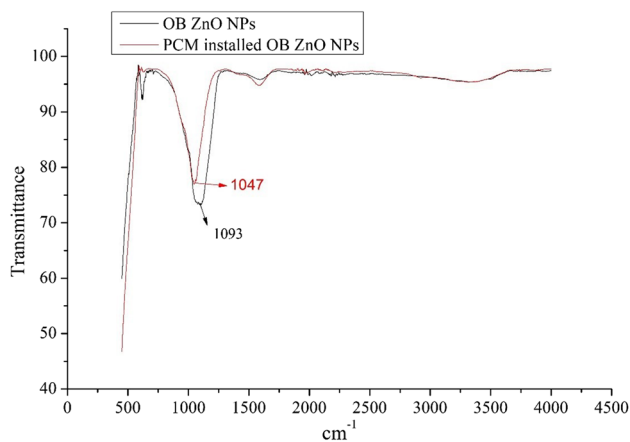
Fig. 6 FTIR diagram of OB-ZnO NPs before and after reaction

Other peaks that do not belong to ZnO in the XRD pattern of BA-ZnO NPs are due to the phytochemicals present in the plant extract that are responsible for reduction and coating [60, 61]. The dimension of the crystallite of the green synthesis OB-ZnO NPs was calculated using Bragg's law (=2dsin) and the Debye-Scherrer equation, following equation numbered 3:

$$D = \frac{K\lambda}{(\beta\cos\Theta}$$ (3)

while D represents particle size (nm), K fixed as 0.89, λ wavelength X-ray fixed as 1.5406 (Å), β the half of value of the highest peak 18.13° (radians) (FWHM = 0.483), and θ angle of fracture.

According to this equation, the size of the nanoparticles was found to be 30.39 nm. In similar studies, it has been determined that they have approximately similar XRD results and cubic structures [62–65].

3.3 Brunauer–Emmett–Teller (BET)

For BET, if larger holes are present in micropore materials, which absorb more N_2 at relatively low pressures, the curve may reach a limiting value or increase when the ratio is close to 1. According to Figure 3, the N_2 adsorption-desorption isotherm of the created adsorbent can be categorized as a type I isotherm. In this diagram, the adsorption isotherm directly touched the P/Po = 1 line. According to Table 3, the OB-ZnO NP-specific surface area based on the BET surface area analyzer is 13.82 m^2/g. Additionally, the BJH measured an average pore width of 30.39 nm and the total pore size of 0.0475 cm^3/g. OB-ZnO NPs can be compatible with the mesoporous structure because its average pore size was in the range of 2 to 50 nm according to Figure 3 [66–69].

3.4 Scanning electron microscopy and energy dispersive X-ray (SEM–EDX)

Scanning electron microscopy (SEM) is an important technique for studying the textural structure, surface morphology, structure, and particle size of an adsorbent. Figure 4 SEM images of synthesized OB-ZnO NPs adsorbent were taken as images at different magnifications such as 10,000–50,000. The photographs show the similarity of microparticles with an average particle size of 100 nm–1 μm. And it shows that the outer surface of the OB-ZnO NP powder is composed of interconnected rod-like particles and small flower forms, forming holes, thus forming an image. As can be seen in the structure, the large surface area of the perforated structures increases the adsorbing capacity. Elemental compositions of OB-ZnO NPs were determined using EDX analysis as shown in Figure 5. The presence of zinc was confirmed at 1.0, 8.7, and 9.2 eV, which is typical for the absorption of metallic ZnO NPs nanocrystalline due to surface plasmon resonance according to the EDX spectrum. Besides Zn and O peaks, weak signals from C, S, O, Ca, and K elements were also detected. It can be said that these weak signals come from the plant extract and the Ca and K peaks come from the water. The composition of each element in the prepared material is shown in Figures 4 and 5. As a result of the reaction, when the SEM-EDX analysis is examined, the presence of nitrogen in the structure of the adsorbing substance PCM and an increase in the amount of oxygen show that the accuracy of the adsorbing process is clear. It is consistent with previous work on the synthesis of ZnO NPs [70–72].

3.5 Fourier-transform infrared spectroscopy (FT-IR)

FT-IR spectrophotometric measurements of OB-ZnO NPs before and after adsorption were made and presented in Fig. 6. OB-Zn ONPs were used to detect the phytochemicals responsible for adsorption. In this study, it was determined that FT-IR, as capping and stabilizing agents, recorded different bands for the functional groups of phytochemical compounds responsible for the biosynthesis of OB-ZnO NPs. Bands and functional groups in the biosynthesis of OB-ZnO NPs were analyzed using FTIR. The 3280 cm^{-1} peak that is evident before the reaction is –OH or –NH, the peak at 1600 cm^{-1} is carbonyl C=O or N=O, the peak at 1093 cm^{-1} belongs to the Ar–O–Ar or Amid II band, and the peak at 615 cm^{-1}. It is thought that the peak at cm^{-1} may belong to –CH due to aromatic groups. Post-reaction shifts occurred in these prominent peaks detected in the zinc nanoparticle. This result clearly shows that the adsorption process, that is, the binding, is on these groups. As a result,
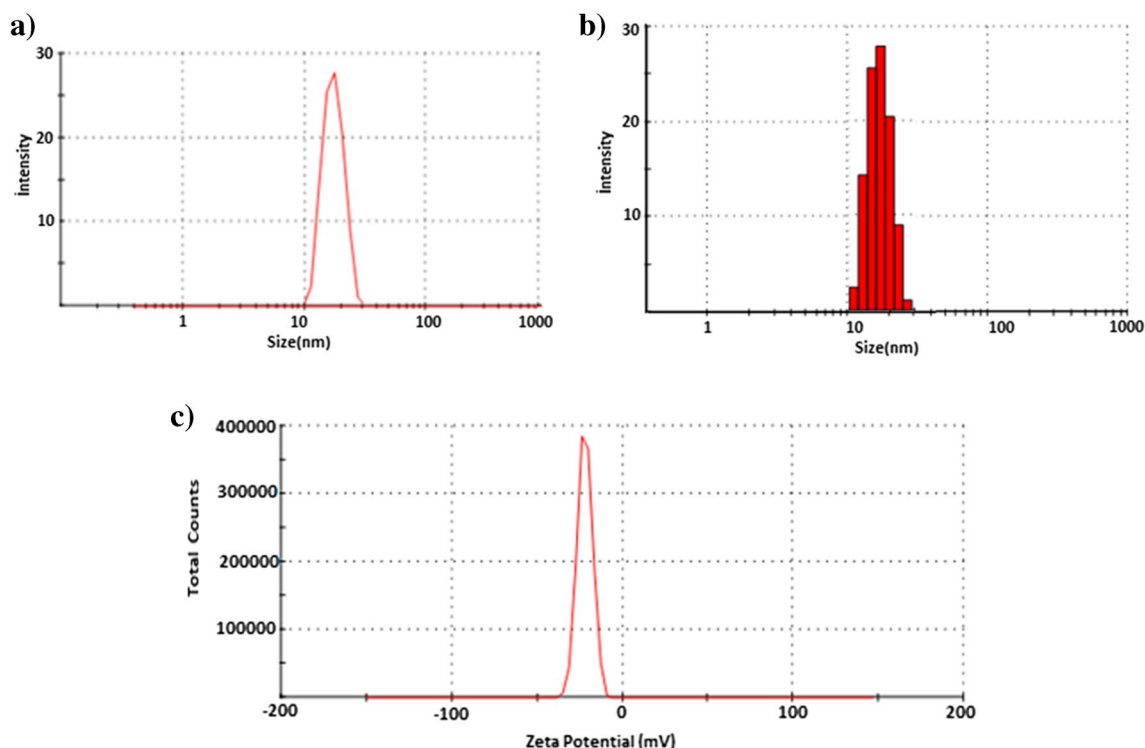
Fig. 7 DLS particle size distribution (**a**, **b**) and zeta potential (**c**) of synthesized OB-ZnO NPs

the disappearance of the peak at 615 and the higher shift on the peak at 1093 clearly indicate that the binding is on these groups. [73–75].

3.6 Dynamic light scattering (DLS), Zetasizer

OB-ZnO NP size distribution image (DLS) oxide nanoparticle is shown in Fig. 7a and b. It is clearly seen in Fig. 6 that the size distribution of the observed zinc oxide nanoparticles ranges from 10 to 40 nm to the medium. The zeta potential of biosynthesized OB-ZnO NPs was found to have a distinct

peak at -22.1 mV, indicating that the nanoparticles are dispersed. This result shows that the synthesized nanoparticles are negatively charged and that the phytochemicals present in the plant extract also play a role in the reaction. A negative zeta potential value indicates that the nanoparticles are negatively charged and takes part in adsorption processes. Despite negative values, it is associated with the stability of moderately dispersed nanoparticles in the medium [76, 77].
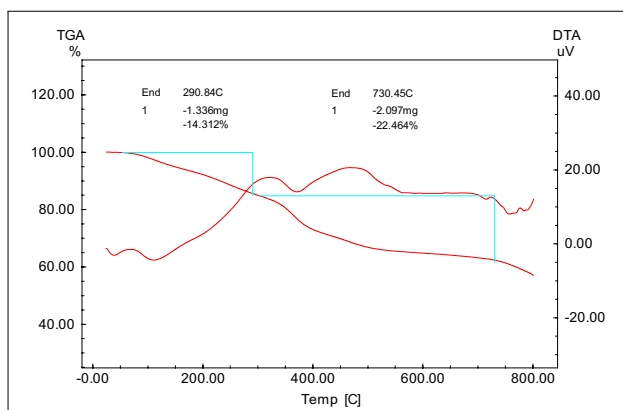

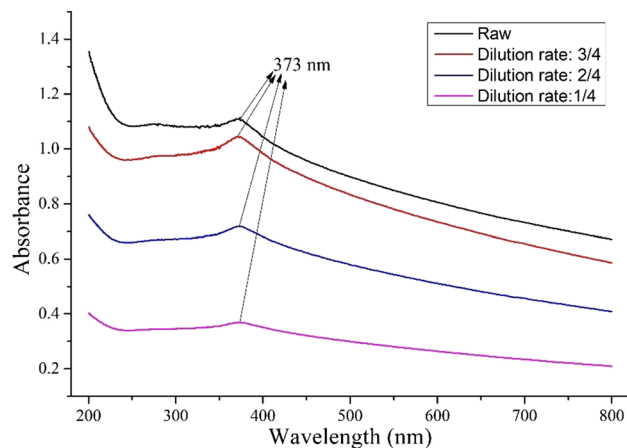**Fig. 8** Temperature-dependent TGA-DTA curve of OB-ZnO NPs

Fig. 9 UV-vis spectra of OB-ZnO NPs

Table 6 Comparison of the obtained values with the literature

|	This study	[92]	[93]	[94]	[96]	[97]	[98]	[99]	[95]
NP chemical	ZnO	ZnO	ZnO	ZnO	ZnO	Zn-Al-CO$_3$	ZnO	MgO	ZnO
NP origin	Ocimum basilicum	Arachis hypogaea	Zeolitic imidazolate	–	Guava leaves	–	–	–	–
BET-surface area (m^2/g)	13.826	–	37.674	8–40	119.12	–	–	1236	5.24
Crystalline size (nm)	30.39	68.61	27–47	30–100	26.8–32.6	0.31–2.29	–	<50	5
Experiment volume (mL)	25	10 mL	25 mL		25	250	10		10
Mixing speed (rpm)	140	–	200	–		–	600	–	–
Experiment time (min)	1–800	15–180	100	500	100	360	150	15–120	180
Working pH's	3–11	1–14	2–12	3, 7, 9	2–10	–	4–8	2–11	4
Optimum pH	5	4	–	9	–	–	4, 8	6	4
Working temp. (°C)	25	Room	25	–	25–45	–	25	Room	25
Pollutant type removed	Paracetamol	Opthalmic, ciprofloxacin	Acid red 57, Remazole red	Tetracycline, ibuprofen	Ibuprofen	Salicylic acid	Ciprofloxacin + ofloxacin, diclofenac + paracetamol	Ciprofloxacin	Ciprofloxacin
Initial concentrations (mg/L)	12.5–200	10–100	3.7×10^{-5} – 3.63×10^{-3} M	0.5–60	$2.76\,10^{-4}$ – $1.7\,10^{-3}$ mol/L	30	mix–20–40	10–250	80
Adsorption capacity (mg/g)	23	8.07	1.26–1.368 mmol/g	2.0–10.0	1.78 mmol/g	21.99–28.37	2.03–2.07	3.6	6.1–6.24
Adsorbent amount (g/L)	0.5	10	0.4–4.0	–	0.8	1.0	10	0.1–1	5.2
pH-adjusting agent	0.1 M H$_2$SO$_4$/ NaOH	0.1 M HCl/ NaOH	0.1 mol/L HCl/ NaOH	–	–	–	0.1M HCl/NaOH	0.1 N HCl/ NaOH	0.1M HCl/ NaOH
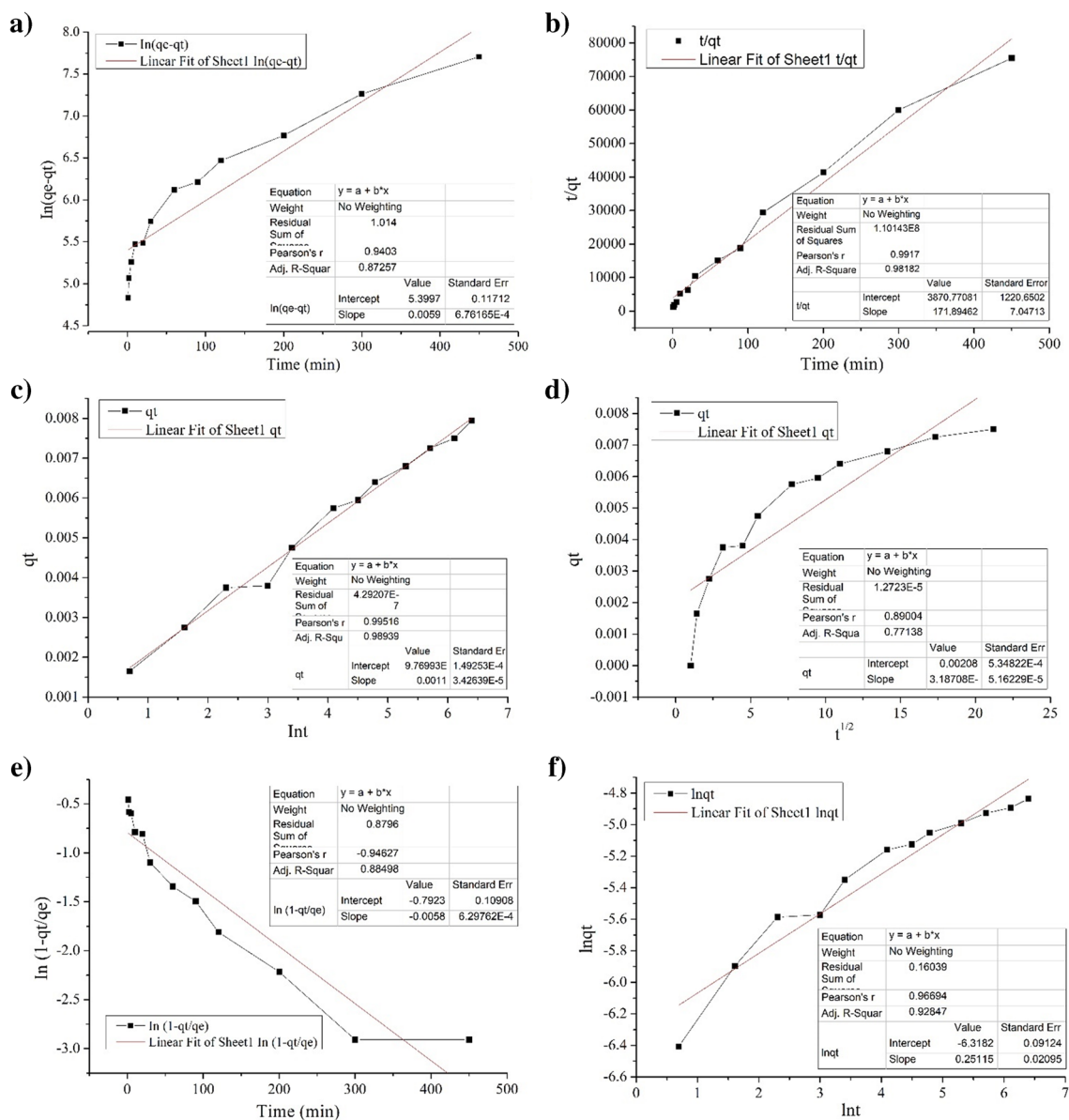
Fig. 10 Regression curves of each kinetic model (**a** pseudo first order, **b** pseudo second order, **c** Elovich, **d** intra-particle diffusion, **e** liquid film diffusion, **f** Bangham)

3.7 Thermogravimetry—differential thermal analysis (TGA-DTA)

DSC-TGA analysis of OB-ZnO NPs of biological origin was carried out to examine the thermal phenomena occurring in the sample while it was heated from room temperature to 9000 °C. TGA of the synthesized samples was carried out by heating under N_2 gas in an alumina crucible at 10 °C min^{-1} in atmospheric air. The DTA-TGA curve of OB-ZnO NPs synthesized from basil stalk extract is shown in Figure 8. It is seen in Figure 8 that the mass percent loss of the different temperature curves in the sample is 14.31% at 25–290 °C, and the mass percent loss at 290–730 °C is 22.464%. This

shows that 33% of the obtained OB-ZnO NPs still experience mass loss up to about 750 °C, and in this case, the obtained nanomaterial is durable at high temperatures. The results obtained are in good agreement with the available literature [68, 78, 79].

3.8 UV–vis spectroscopy

In current bio-assisted synthesis protocols, the reaction is mixed with OB aqueous sap extract and zinc nitrate salt (1:3) and allowed to react. When the color change was observed after 30 min, the measurement was taken on the UV-vis spectrophotometer (Hach DR6000), and the maximum

formation wavelength was determined and presented in Figure 8. The observed color change was due to surface excitation, which is the plasmon resonance of the OB-ZnO NPs, with a peak at 373 nm. In the literature, it has been reported that the UV-vis spectra taken for the zinc oxide nanoparticle biosynthesized using *Solanum torvum* show a maximum absorption peak at 373 nm (Figure 9). There is a characteristic peak for OB-ZnO NPs synthesized in our study, and it is believed to be spherical in a single sharp absorbance condition in the same direction as stated in Mei's theory [80, 81].

3.9 Adsorptive removal of PCM

3.9.1 Adsorption kinetics

In order to access general information about the basic mechanisms of adsorption, it is necessary to make a kinetic evaluation. In this way, it is learned how long the reaction took place and the step of the pollutant adsorbing rate is determined [82]. In this study, 6 different models were studied to make a kinetic evaluation, and the results are summarized in Table 4. On the other hand, the regression curves of each of the models are presented in Fig. 10. On the other hand, the graph showing the total amount of pollutant removed per unit adsorbent obtained in experimental studies and the change of values calculated from kinetic models against time is presented in Fig. 11.

The yields and q_e values obtained under equilibrium conditions at pH 3, 5, 7, 9, and 11 were calculated as 16.74, 16.91, 16.89, 16.82, and 14.88 mg/g, respectively. In this context, although the highest removal is seen at pH 5, the natural pH of the solution is around 6, the difference in removal efficiency is not very high, and kinetic and isotherm studies were carried out at this pH in order to avoid unnecessary acid consumption for this difference. Accordingly, R^2 values of pseudo first order, Intra-particle diffusion, liquid film diffusion, and Bangham models were obtained as 0.873, 0.771, 0.885 and 0.9929, respectively. The R^2 value of the Elovich model was found to be 0.989, while that of the pseudo second order model was calculated as 0.982. If the SAE value, which is expressed as the sum of the absolute errors between the values calculated with the experimental results, is examined, it is calculated as 0.003 for Elovich and 0.04 for the pseudo second order. Again, the HYBRID values calculated as the division of the SSE values by the predicted value were calculated as 16.898 for the pseudo second order and 0.920 for the Elovich. Again, in a similar situation, X^2, which is the ratio of the square of the difference between the values calculated with the experimental results and defined as the non-linear chi-square test, to the calculated values, was calculated as 0.001 for the pseudo second order but 0 for the Elovich. When the literature was examined, the Elovich

kinetics model was suitable with an R^2 value of 0.990 in the study in which Hg removal was performed with graphene oxide–iron magnetic nanoparticle [83]. In addition, in the study in which tetracycline removal was performed by incorporating ferroferric oxide into powdered activated carbon, it was determined that the Elovich kinetics model was suitable with an R^2 value of 0.996 [84]. In addition, in a study in which nitrate removal was performed only with ZnO NP and with chitosan-polystyrens Zn NP, 4.2 mg/g NO_3 removal efficiency was achieved with only ZnO NP and 0.45 mg/g NO_3 removal efficiency with chitosan-polystyrens Zn NP, and R^2 values of 0.999 and 0.988 were achieved with both NPs. It has been revealed that the most appropriate kinetic model is Elovich [85]. In the Elovich model, it is stated that there is a chemical adsorption mechanism, and as a result of the contaminant covering the adsorbent surface, the adsorption rate decreases over time, that is, the adsorption rate decreases exponentially as the amount of adsorbed pollutant increases [86, 87]. Therefore, the amount of adsorption of PCM ions on OB-ZnO NP decreased with time.

3.9.2 Adsorption isotherms

Various isotherms are used to explain the relationship between pollutant and adsorbent at stable conditions in adsorption. In this way, the specifications of the surface to which the contaminant adheres are determined. Six of the isotherms frequently used in water quality applications were used in our study, and the results are summarized in Table 5. On the other hand, the regression curves of each of the isotherm's models are presented in Figure 12. On the other hand, the graph showing the change in the amount of pollutant removed per unit adsorbent obtained in the experimental studies and the values calculated from the kinetic
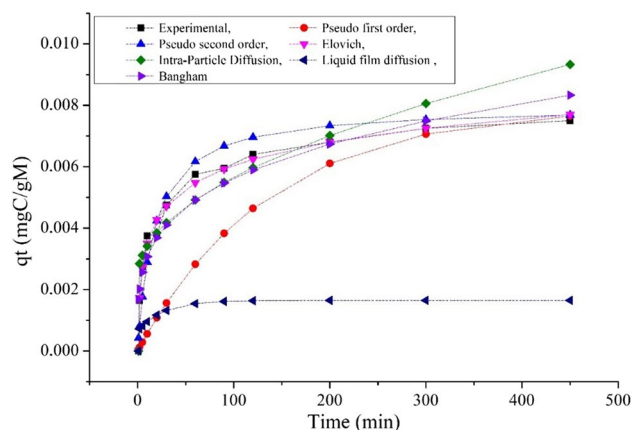

Fig. 11 Graph of change of kinetic evaluation experimental and theoretical removal efficiencies versus time
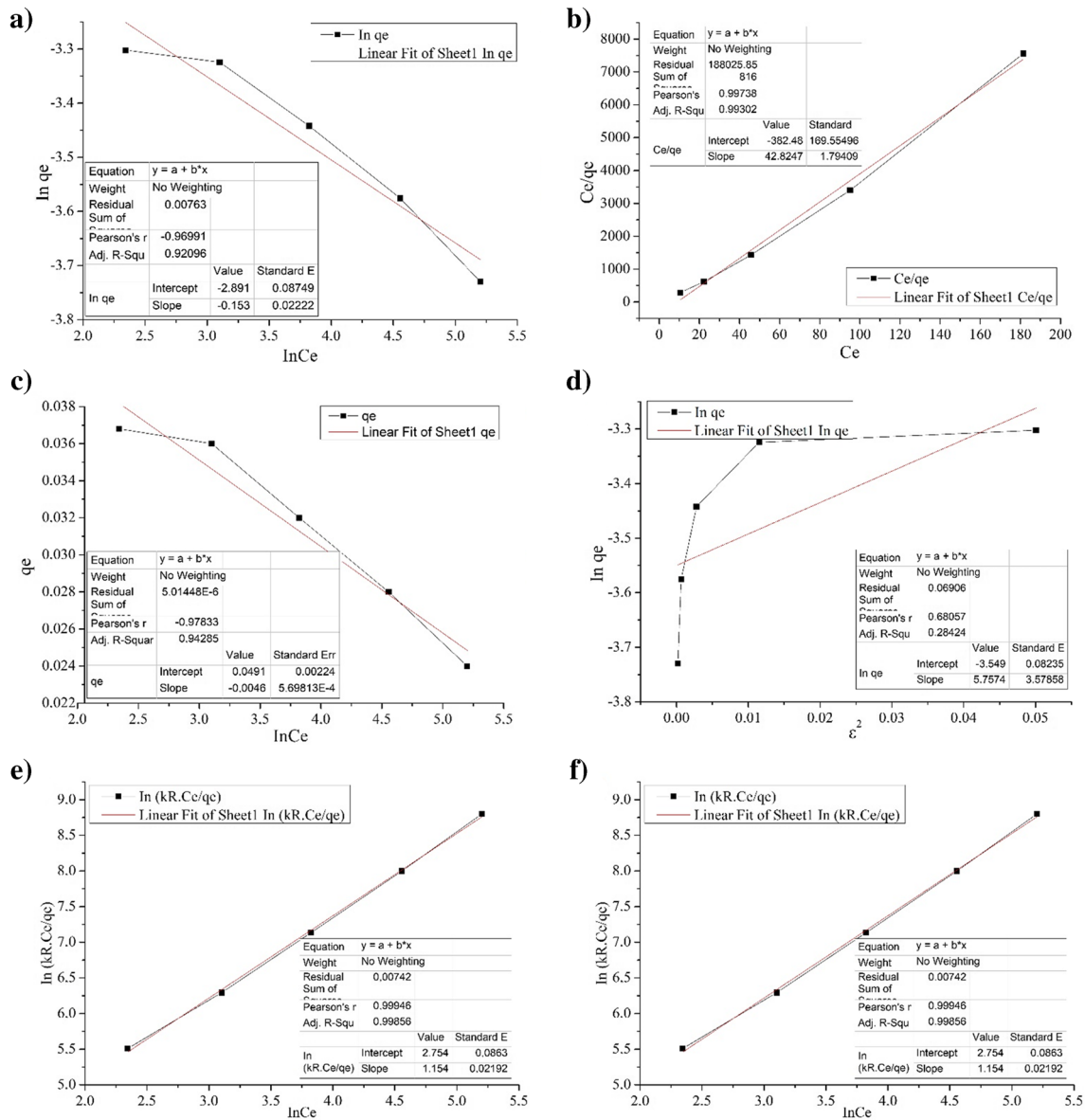
Fig. 12 Linear regression curves of any isotherm model **a** Freundlich, **b** Langmuir, **c** Temkin, **d** Dubinin–Redushkevich, **e** Redlich-Peterson, **f** Sips

models, against the equilibrium concentration, is presented in Figure 13.

If the results are examined, the R^2 value of the Dubinin-Radushkevich model is quite low (0.284) compared to the others. On the other hand, R^2 values of Freundlich and Temkin models were calculated as 0.921 and 0.943, respectively. However, the R^2 value of the Redlich-Peterson and Sips model was calculated as 0.999. Error functions were used to choose the most appropriate model [88]. When looking at the diversity (SSE) between the data, this value is 0.005 in the Sips model, but 0 in the Redlich-Peterson model. In addition, when the sum of absolute errors (SAE) between the values calculated with the experimental results is examined,

it is found to be 0.157 in the Sips model and 0.006 in the Redlich-Peterson model. In addition, when the ratio of the square of the difference between the data in the experiments and the calculated values (non-linear chi-square test, X^2) was calculated as 0 in the Redlich-Peterson model. Moreover, if the ARE, HYBRID, and MPSD values are examined, it is clear that these values are higher in the Sips model. Therefore, when looking at the error functions as well as the R^2 value in choosing the best model, it can be seen that the most suitable model for our study is the Redlich-Peterson model. When the literature was examined, the Freundlich and Redlich-Peterson models were calculated as the most suitable model with an R^2 value of 0.867 in the reaction with
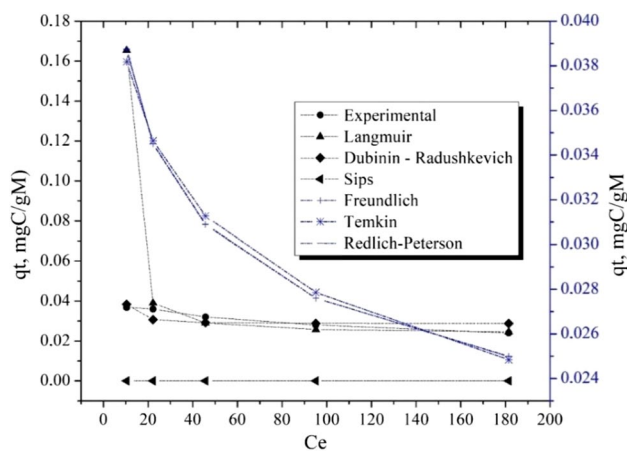
Fig. 13 Graphical representation of Ce value versus q_e values obtained experimentally and theoretically in isotherm evaluation

5.03 mg/g removal efficiency in the study in which phosphate adsorption on magnetic iron oxide NP was examined [89]. On the other hand, in the study examining the adsorption of heavy metals on chitosan nanofibers, NP functionalized with TiO_2; the Redlich-Peterson model was found to be suitable with the highest R^2 value of 0.991 [90]. In another study, the adsorption of Co(II) with NiO NP with a size of 30–40 nm was performed, and the Redlich-Peterson model was evaluated as the most suitable model with an R^2 value of 0.99 [91]. In our study, it is stated that the most suitable model for PCM removal of OB-ZnO NP is the Redlich-Peterson model with an R^2 value of 0.999, and the single-layer reaction of OB-ZnO NP is the dominant reaction in removing PCM ions [90].

3.9.3 Adsorption mechanism

The produced OB-ZnO NPs were not soluble in water, and as can be seen from the pH_{pzc} values, in the optimum adsorption observed at lower pH values between 2.0 and 8.0, the electrostatic interaction ensured that the biosynthesized NPs had too much activity on paracetamol adsorption. Therefore, intermolecular mechanisms such as bonding and van der Waals transfers, which are not affected by charged species in distribution, likely govern the adsorption of paracetamol [23].

3.10 General assessment on removal efficiencies

The summary of the treatment studies with nanoparticles in the literature is presented in Table 6. The particle size of OB-ZnO NP obtained from the *Arachis hypogaea* plant was measured as 68.61 nm, and ophthalmic and ciprofloxacin drugs were removed with this product. While the use of 10 g/L adsorbent was reported in the adsorption experiment at

room temperature, it was reported that the drug concentration removed per unit adsorbent was 8.07 mg/g [92]. On the other hand, the particle size of the NP obtained by ZnO coating on the zeolite material was measured in the range of 27–47 nm, and it was reported that the removal efficiency of Acid red 57 and Remazol red dyes was high with this product [93]. In addition, in a different study with Zn-coated NP, the photocatalyst and adsorptive properties of NP were investigated. In the study, in which products with a surface area of 8–40 m^2/g and a size of 30–100 nm were obtained, tetracycline and ibuprofen were removed from pharmaceutical wastes, and it was reported that a removal efficiency of 2–10 mg/g was reached and NP also had photocatalytic properties [94]. On the other hand, in the study where the removal efficiency of ciprofloxacin from the continuous fed system of ZnO was examined, it was reported that 6.1 mg/g removal efficiency was reached, and the application and operation were easy [95].

On the other hand, chitosan-reinforced Fe-NPs with a size of 15–20 nm were synthesized. In a study in which bisphenol-A removal was performed with these, it was reported that a removal efficiency of 65.16 mg/g was achieved [100]. On the other hand, in the adsorption study where the removal of 2 types of neutral aromatic carbamazepine was carried out with a lignin-based composite nanoparticle, it was reported that a removal efficiency of 91–150 mg/g was achieved thanks to the functional groups of the nanoparticle [101]. In addition, hematite-derived nanoparticles were produced, and particles with a size of 15–41 nm were obtained. In a study where carbamazepine was removed with these, it was reported that a removal efficiency of 2.89 mg/g was achieved [102]. In our study, the surface area of OB-ZnO NP obtained from OB plant wastes was measured as 13.826 m^2/g, the maximum particle diameter was 30.39 nm, and the PCM removal efficiency was calculated as 23 mg/g.

4 Conclusions

The results obtained in this study, in which the characterization of OB-ZnO NPs produced in OB plant wastes and adsorption tests for PCM removal were performed, are briefly listed below:

– It was calculated that the size distribution of OB-ZnO NPs ranged from 10 to 40 nm to medium and the average size was 30.39 nm.
– BET surface area analyzer of OB-ZnO NPs is 13.826 m^2/g and total pore size of 0.0475 cm^3/g.
– The zeta potential of biosynthesized OB-ZnO NPs is −22.1 mV.

- Since OB-ZnO NPs experience a mass loss of 33% at about 750 °C, these NPs show that they are durable at high temperatures.
- Six different kinetic and isotherm models are studied and used in error function tests to compare kinetics and isotherms.
- The most suitable kinetic model for PCM removal with synthesized OB-ZnO NPs was Elovich with an R^2 value of 0.989, and the most suitable isotherm model was Redlich-Peterson with an R^2 value of 0.999.
- The amount of PCM removed per unit of OB-ZnO NP was calculated as 23 mg/g.

This study shows that ZnO NPs obtained from waste OB plant are effective in PCM removal.

Data availability The datasets generated during and/or analyzed during the current study are available from the corresponding author on reasonable request.

Declarations

Ethical approval All authors have read, understood, and have complied as applicable with the statement on "Ethical responsibilities of Authors" as found in the Instructions for Authors and are aware that with minor exceptions, no changes can be made to authorship once the paper is submitted.

Consent to participate All authors have given consent to their contribution.

Consent for publication All authors have agreed with the content and all have given explicit consent to publish.

Competing interests The authors declare no competing interests.

References

1. Falkenmark M (2022) Planning of Africa's land/water future: hard or soft landing? Ambio 51:9–12. https://doi.org/10.1007/s13280-021-01527-9
2. Zur J, Wojcieszy D, Hupert-Kocurek K et al (2018) Paracetamole toxicity and microbial utilization. Pseudomonas moorei KB4 as a case study for exploring degradation pathway. Chemosphere 206:192–202. https://doi.org/10.1016/j.chemosphere.2018.04.179
3. García-Mateos FJ, Ruiz-Rosas R, Marqués MD, Cotoruelo L (2015) Removal of paracetamol on biomass-derived activated carbon: modeling the fixed bed breakthrough curves using batch adsorption experiments. Chem Eng J 279:18–30
4. Phong Vo HN, Le GK, Hong Nguyen TM et al (2019) Acetaminophen micropollutant: historical and current occurrences, toxicity, removal strategies and transformation pathways in different environments. Chemosphere 236:1–15. https://doi.org/10.1016/J.CHEMOSPHERE.2019.124391
5. Chacón FJ, Cayuela ML, Sánchez-Monedero MA (2022) Paracetamol degradation pathways in soil after biochar addition. Environmental Pollution 307:. https://doi.org/10.1016/j.envpol.2022.119546
6. Edrees W, Yusuf Q, Abdullah M et al (2017) A review on comparative study between the physicochemical and biological processes for paracetamol degradation. Univ J Pharm Res 2:18–27
7. An J, Zhou Q, Sun F, Zhang L (2009) Ecotoxicological effects of paracetamol on seed germination and seedling development of wheat (Triticum aestivum L.). J Hazard Mater 169:751–757. https://doi.org/10.1016/j.jhazmat.2009.04.011
8. Guiloski IC, Luiz J, Ribas C et al (2017) Paracetamol causes endocrine disruption and hepatotoxicity in male fish Rhamdia quelen after subchronic exposure. Environ Toxicol Pharmacol 53:111–120. https://doi.org/10.1016/j.etap.2017.05.005
9. Piedade F, Bio S, Nunes B (2020) Effects of common pharmaceutical drugs (paracetamol and acetylsalicylic acid) short term exposure on biomarkers of the mussel Mytilus spp. Environ Toxicol Pharmacol 73:. https://doi.org/10.1016/J.ETAP.2019.103276
10. Giménez V, Nunes B (2019) Effects of commonly used therapeutic drugs, paracetamol, and acetylsalicylic acid, on key physiological traits of the sea snail Gibbula umbilicalis. Brain Imaging Behav 26:21858–21870. https://doi.org/10.1007/s11356-019-04653-w
11. Campanha MB, Taj Awan A, de Sousa DNR et al (2015) A 3-year study on occurrence of emerging contaminants in an urban stream of São Paulo State of Southeast Brazil. Environ Sci Pollut Res 22:7936–7947. https://doi.org/10.1007/s11356-014-3929-x
12. Lolić A, Paíga P, Santos LHMLM et al (2015) Assessment of non-steroidal anti-inflammatory and analgesic pharmaceuticals in seawaters of north of Portugal: occurrence and environmental risk. Sci Total Environ 508:240–250. https://doi.org/10.1016/J.SCITOTENV.2014.11.097
13. Birch GF, Drage DS, Thompson K et al (2015) Emerging contaminants (pharmaceuticals, personal care products, a food additive and pesticides) in waters of Sydney estuary, Australia. Mar Pollut Bull 97:56–66. https://doi.org/10.1016/j.marpolbul.2015.06.038
14. Nieto-Juárez JI, Torres-Palma RA, Botero-Coy AM, Hernández F (2021) Pharmaceuticals and environmental risk assessment in municipal wastewater treatment plants and rivers from Peru.

Environ Int 155:106674. https://doi.org/10.1016/J.ENVINT.2021.106674

15. Wang J, Wang S (2016) Removal of pharmaceuticals and personal care products (PPCPs) from wastewater: a review. J Environ Manage 182:620–640. https://doi.org/10.1016/j.jenvman.2016.07.049

16. Khan AH, Khan NA, Ahmed S et al (2020) Application of advanced oxidation processes followed by different treatment technologies for hospital wastewater treatment. J Clean Prod 269:122411. https://doi.org/10.1016/j.jclepro.2020.122411

17. Pacheco-Álvarez M, Picos Benítez R, Rodríguez-Narváez OM et al (2022) A critical review on paracetamol removal from different aqueous matrices by Fenton and Fenton-based processes, and their combined methods. Chemosphere 303:134883. https://doi.org/10.1016/J.CHEMOSPHERE.2022.134883

18. Pilli S, Sellamuthu B, Pandey AK, Tyagi RD (2020) Treatment of wastewater containing pharmaceuticals: biological treatment. In: Current developments in biotechnology and bioengineering. Elsevier, pp 463–520

19. Chu KH, Al-Hamadani YAJ, Park CM et al (2017) Ultrasonic treatment of endocrine disrupting compounds, pharmaceuticals, and personal care products in water: a review. Chem Eng J 327:629–647. https://doi.org/10.1016/j.cej.2017.06.137

20. Vieira WT, de Farias MB, Spaolonzi MP et al (2020) Removal of endocrine disruptors in waters by adsorption, membrane filtration and biodegradation. A review. Environ Chem Lett 18:1113–1143. https://doi.org/10.1007/s10311-020-01000-1

21. Nadour M, Boukraa F, Benaboura A (2019) Removal of diclofenac, paracetamol and metronidazole using a carbon-polymeric membrane. J Environ Chem Eng 7:. https://doi.org/10.1016/J.JECE.2019.103080

22. Elamin MR, Abdulkhair BY, Algethami FK, Khezami L (2021) Linear and nonlinear investigations for the adsorption of paracetamol and metformin from water on acid-treated clay. Sci Rep 11:13606–13619. https://doi.org/10.1038/s41598-021-93040-y

23. Akpomie KG, Conradie J (2023) Efficient adsorptive removal of paracetamol and thiazolyl blue from polluted water onto biosynthesized copper oxide nanoparticles. Sci Rep 13:859–874. https://doi.org/10.1038/s41598-023-28122-0

24. Hoseinpour V, Ghaemi N (2018) Green synthesis of manganese nanoparticles: applications and future perspective-a review. J Photochem Photobiol B 189:234–243. https://doi.org/10.1016/j.jphotobiol.2018.10.022

25. Hussain I, Singh NB, Singh A et al (2016) Green synthesis of nanoparticles and its potential application. Biotechnol Lett 38:545–560. https://doi.org/10.1007/s10529-015-2026-7

26. Gour A, Jain NK (2019) Advances in green synthesis of nanoparticles. Artif Cells Nanomed Biotechnol 47:844–851. https://doi.org/10.1080/21691401.2019.1577878

27. Ramesh P, Rajendran A, Meenakshisundaram M (2014) Green synthesis of zinc oxide nanoparticles using flower extract Cassia auriculata. J Nanosci Nanotechnol 1:41–45

28. Qanash H, Bazaid AS, Alharazi T et al (2023) Bioenvironmental applications of myco-created bioactive zinc oxide nanoparticle-doped selenium oxide nanoparticles. Biomass Convers Biorefin. https://doi.org/10.1007/s13399-023-03809-6

29. Kumari P, Alam M, Siddiqi WA (2019) Usage of nanoparticles as adsorbents for waste water treatment: an emerging trend. Sustain Mater Technol 22:128–142. https://doi.org/10.1016/j.susmat.2019.e00128

30. Raghavendra VB, Shankar S, Govindappa M et al (2022) Green synthesis of zinc oxide nanoparticles (ZnO NPs) for effective degradation of dye, polyethylene and antibacterial performance in waste water treatment. J Inorg Organomet Polym Mater 32:614–630. https://doi.org/10.1007/s10904-021-02142-7

31. Vidya C, Manjunatha C, Chandraprabha M et al (2017) Hazard free green synthesis of ZnO nano-photo-catalyst using Artocarpus heterophyllus leaf extract for the degradation of Congo red dye in water treatment applications. J Environ Chem Eng 5:3172–3180. https://doi.org/10.1016/j.jece.2017.05.058

32. Rajendar V, Shilpa Chakra CH, Rajitha B et al (2017) Effect of TWEEN 80 on the morphology and antibacterial properties of ZnO nanoparticles. J Mater Scie: Mater Electron 28:3272–3277. https://doi.org/10.1007/s10854-016-5919-x

33. Ahmed S, Ali Chaudhry S, Ikram S (2016) A review on biogenic synthesis of ZnO nanoparticles using plant extracts and microbes: a prospect towards green chemistry. https://doi.org/10.1016/j.jphotobiol.2016.12.011

34. Tan W, Du W, Darrouzet-Nardi AJ et al (2018) Effects of the exposure of TiO2 nanoparticles on basil (Ocimum basilicum) for two generations. Sci Total Environ 636:240–248. https://doi.org/10.1016/j.scitotenv.2018.04.263

35. Pirtarighat S, Ghannadnia M, Baghshahi S (2019) Biosynthesis of silver nanoparticles using Ocimum basilicum cultured under controlled conditions for bactericidal application. Mater Sci Eng C 98:250–255. https://doi.org/10.1016/j.msec.2018.12.090

36. Malapermal V, Botha I, Krishna SBN, Mbatha JN (2017) Enhancing antidiabetic and antimicrobial performance of Ocimum basilicum, and Ocimum sanctum (L.) using silver nanoparticles. Saudi J Biol Sci 24:1294–1305. https://doi.org/10.1016/j.sjbs.2015.06.026

37. Rahman A, Harunsani MH, Tan AL, Khan MM (2021) Zinc oxide and zinc oxide-based nanostructures: biogenic and phytogenic synthesis, properties and applications. Springer, Berlin Heidelberg

38. Umavathi S, Subash M, Gopinath K et al (2021) Facile synthesis and characterization of ZnO nanoparticles using Abutilon indicum leaf extract: an eco-friendly nano-drug on human microbial pathogens. J Drug Deliv Sci Technol 66:102917. https://doi.org/10.1016/j.jddst.2021.102917

39. Cao Y, Dhahad HA, El-Shorbagy MA et al (2021) Green synthesis of bimetallic ZnO–CuO nanoparticles and their cytotoxicity properties. Sci Rep 11:1–8. https://doi.org/10.1038/s41598-021-02937-1

40. Zhu W, Hu C, Ren Y et al (2021) Green synthesis of zinc oxide nanoparticles using Cinnamomum camphora (L.) Presl leaf extracts and its antifungal activity. J Environ Chem Eng 9:106659. https://doi.org/10.1016/j.jece.2021.106659

41. Rajivgandhi G, Mythili Gnanamangai B, Heela Prabha T et al (2022) Biosynthesized zinc oxide nanoparticles (ZnO NPs) using actinomycetes enhance the anti-bacterial efficacy against K. Pneumoniae J King Saud Univ Sci 34:101731. https://doi.org/10.1016/j.jksus.2021.101731

42. Lagergren SK (1898) About the theory of so-called adsorption of soluble substances. Sven Vetenskapsakad Handingarl 24:1–39

43. Ho YS, Wase' D, Forster CF (1996) Removal of lead ions from aqueous solution using sphagnum moss peat as adsorbent. Water SA 22:214–219

44. Kumar PS, Ramalingam S, Kirupha SD et al (2011) Adsorption behavior of nickel(II) onto cashew nut shell: equilibrium, thermodynamics, kinetics, mechanism and process design. Chem Eng J 167:122–131. https://doi.org/10.1016/J.CEJ.2010.12.010

45. Boyd GE, Adamson AW, Myers LS (1947) The exchange adsorption of ions from aqueous solutions by organic zeolites. II. Kinetics. J Am Chem Soc 69:2836–2848. https://doi.org/10.1021/JA01203A066/ASSET/JA01203A066.FP.PNG_V03

46. Chen L, Zuo L, Jiang Z et al (2019) Mechanisms of shale gas adsorption: evidence from thermodynamics and kinetics study of methane adsorption on shale. Chem Eng J 361:559–570. https://doi.org/10.1016/j.cej.2018.11.185

47. Freundlich HMF (1906) Over the adsorption in solution. J Phys Chem 57:1100–1107

48. Jeppu GP, Clement TP (2012) A modified Langmuir-Freundlich isotherm model for simulating pH-dependent adsorption effects. J Contam Hydrol 129–130:46–53. https://doi.org/10.1016/J.JCONHYD.2011.12.001

49. Langmuir I (1916) The constitution and fundamental properties of solids and liquids. Part I. Solids. J Am Chem Soc 38:2221–2295. https://doi.org/10.1021/JA02268A002/ASSET/JA02268A002.FP.PNG_V03

50. Temkin MI (1940) Kinetics of ammonia synthesis on promoted iron catalysts. Acta Physiochim 12:327–356

51. Foo KY, Hameed BH (2010) Insights into the modeling of adsorption isotherm systems. Chem Eng J 156:2–10. https://doi.org/10.1016/J.CEJ.2009.09.013

52. Dubinin MM (1975) Physical adsorption of gases and vapors in micropores physical adsorption of gases and vapors in micropores. Prog Surf Membr Sci 9:1–70. https://doi.org/10.1016/B978-0-12-571809-7.50006-1

53. Liu QS, Zheng T, Wang P et al (2010) Adsorption isotherm, kinetic and mechanism studies of some substituted phenols on activated carbon fibers. Chem Eng J 157:348–356. https://doi.org/10.1016/J.CEJ.2009.11.013

54. Inglezakis VJ, Poulopoulos SG, Kazemian H (2018) Insights into the S-shaped sorption isotherms and their dimensionless forms. Microporous Mesoporous Mater 272:166–176. https://doi.org/10.1016/J.MICROMESO.2018.06.026

55. Ncibi MC (2008) Applicability of some statistical tools to predict optimum adsorption isotherm after linear and non-linear regression analysis. J Hazard Mater 153:207–212. https://doi.org/10.1016/J.JHAZMAT.2007.08.038

56. Subramanyam B, Das A (2014) Linearised and non-linearised isotherm models optimization analysis by error functions and statistical means. J Environ Health Sci Eng 12:. https://doi.org/10.1186/2052-336X-12-92

57. Ng JCY, Cheung WH, McKay G (2002) Equilibrium studies of the sorption of Cu(II) ions onto chitosan. J Colloid Interface Sci 255:64–74. https://doi.org/10.1006/JCIS.2002.8664

58. Kumar KV, Porkodi K, Rocha F (2008) Comparison of various error functions in predicting the optimum isotherm by linear and non-linear regression analysis for the sorption of basic red 9 by activated carbon. J Hazard Mater 150:158–165. https://doi.org/10.1016/J.JHAZMAT.2007.09.020

59. Pandiyan N, Murugesan B, Arumugam M et al (2019) Ionic liquid - a greener templating agent with Justicia adhatoda plant extract assisted green synthesis of morphologically improved Ag-Au/ZnO nanostructure and its antibacterial and anticancer activities. J Photochem Photobiol B 198:111559. https://doi.org/10.1016/j.jphotobiol.2019.111559

60. MuthuKathija M, Sheik Muhideen Badhusha M, Rama V (2023) Green synthesis of zinc oxide nanoparticles using Pisonia alba leaf extract and its antibacterial activity. Applied Surface Science Advances 15:100400. https://doi.org/10.1016/j.apsadv.2023.100400

61. Sivasankarapillai VS, Krishnamoorthy N, Eldesoky GE et al (2023) One-pot green synthesis of ZnO nanoparticles using Scoparia dulcis plant extract for antimicrobial and antioxidant activities. Appl Nanosci 13:6093–6103. https://doi.org/10.1007/s13204-022-02610-7

62. Sampath S, Bhushan M, Saxena V et al (2022) Green synthesis of Ag doped ZnO nanoparticles: study of their structural, optical, thermal and antibacterial properties. Mater Technol 37:2785–2794. https://doi.org/10.1080/10667857.2022.2075307/SUPPL_FILE/YMTE_A_2075307_SM2981.DOCX

63. Keskin C, Baran A, Baran MF et al (2022) Green synthesis, characterization of gold nanomaterials using Gundelia tournefortii

leaf extract, and determination of their nanomedicinal (antibacterial, antifungal, and cytotoxic) potential. J Nanomater 2022:. https://doi.org/10.1155/2022/7211066

64. Baran MF, Acay H (2019) Antimicrobial activity of silver nanoparticles synthesized with extract of tomato plant against bacterial and fungal pathogens. Middle Black Sea J Health Sci 5:67–73. https://doi.org/10.19127/mbsjohs.551132

65. Khan AU, Malik N, Singh B et al (2023) Biosynthesis, and characterization of zinc oxide nanoparticles (ZnONPs) obtained from the extract of waste of strawberry. J Umm Al-Qura Univ Appl Sci 2023:1–8. https://doi.org/10.1007/S43994-023-00038-5

66. Yadav J, Rani M, Shanker U (2023) Green biosynthesized zinc-based nanocomposite for efficient removal of emerging contaminants. Micro Nano Eng 18:100170. https://doi.org/10.1016/j.mne.2022.100170

67. Al-Askar AA, Hashem AH, Elhussieny NI, Saied E (2023) Green biosynthesis of zinc oxide nanoparticles using Pluchea indica leaf extract: antimicrobial and photocatalytic activities. Molecules 28:4679. https://doi.org/10.3390/molecules28124679

68. Yildirim A, Acay H, Baran F (2022) Synthesis and characterisation of mushroom-based nanocomposite and its efficiency on dye biosorption via antimicrobial activity. Int J Environ Anal Chem 102:1545–1562. https://doi.org/10.1080/03067319.2020.1739664

69. Yildirim A, Baran MF, Acay H (2020) Kinetic and isotherm investigation into the removal of heavy metals using a fungal-extract-based bio-nanosorbent. Environ Technol Innov 20:101076. https://doi.org/10.1016/j.eti.2020.101076

70. Yildirim A, Acay H, Baran F (2020) Synthesis and characterisation of mushroom-based nanocomposite and its efficiency on dye biosorption via antimicrobial activity. 102:1545–1562. https://doi.org/10.1080/03067319.2020.1739664

71. Thirumoorthy GS, Balasubramaniam O, Kumaresan P et al (2021) Tetraselmis indica mediated green synthesis of zinc oxide (ZnO) nanoparticles and evaluating its antibacterial, antioxidant, and hemolytic activity. Bionanoscience 11:172–181. https://doi.org/10.1007/s12668-020-00817-y

72. Ezealisiji KM, Siwe-Noundou X, Maduelosi B et al (2019) Green synthesis of zinc oxide nanoparticles using Solanum torvum (L) leaf extract and evaluation of the toxicological profile of the ZnO nanoparticles–hydrogel composite in Wistar albino rats. Int Nano Lett 9:99–107. https://doi.org/10.1007/s40089-018-0263-1

73. Baran MF, Yildirim A, Acay H et al (2022) Adsorption performance of *Bacillus licheniformis* sp. bacteria isolated from the soil of the Tigris River on mercury in aqueous solutions. Int J Environ Anal Chem 102:2013–2028. https://doi.org/10.1080/03067319.2020.1746779

74. Onursal N, Dal MC, Kul AR, Yavuz Ö (2020) Cu (II) iyonlarının aktive edilmiş karışık tipteki kil ile sudan uzaklaştırılması, izoterm, kinetik ve termodinamik parametrelerin incelenmesi. Euroasia J Math Eng Nat Med Sci 8:85–103. https://doi.org/10.38065/euroasiaorg.84

75. Baran M F, Duz M Z, Uzan S et al (2018) Removal of Hg(II) from aqueous solution by Bacillus subtilis ATCC 6051 (B1). J Bioprocess Biotech 08: https://doi.org/10.4172/2155-9821.1000329

76. Noohpisheh Z, Amiri H, Farhadi S, Mohammadi-gholami A (2020) Green synthesis of Ag-ZnO nanocomposites using Trigonella foenum-graecum leaf extract and their antibacterial, antifungal, antioxidant and photocatalytic properties. Spectrochim Acta A Mol Biomol Spectrosc 240:118595. https://doi.org/10.1016/j.saa.2020.118595

77. Salari P, Moghaddam MG, Bahreini M, Sharifmoghadam MR (2023) Green synthesis of ZnO nanoparticles from Foeniculum vulgare Mill. seed extract and its antibacterial effects on food-borne bacteria. J Med Plants 22:14–26

78. Baran MF, Duz MZ (2021) Removal of cadmium (II) in the aqueous solutions by biosorption of *Bacillus licheniformis* isolated from soil in the area of Tigris River. Int J Environ Anal Chem 101:533–548. https://doi.org/10.1080/03067319.2019.1669583

79. Baran MF (2019) Synthesis and antimicrobial applications of silver nanoparticles from Artemisia absinthium plant. Biol Chem Res 6:96–103

80. Chandrasekaran S, Anbazhagan V, Anusuya S (2023) Green route synthesis of ZnO nanoparticles using Senna auriculata aqueous flower extract as reducing agent and evaluation of its antimicrobial, antidiabetic and cytotoxic activity. Appl Biochem Biotechnol 195:3840–3854. https://doi.org/10.1007/s12010-022-03900-0

81. Govindaraj M, Babu S, Rathinam R et al (2023) Integrated electrocoagulation–photoelectrocatalytic oxidation for effective treatments of aqueous solution bisphenol-A using green-synthesized ZnO nanoparticles. Chem Pap 77:169–183. https://doi.org/10.1007/s11696-022-02473-w

82. Gupta VK, Suhas, (2009) Application of low-cost adsorbents for dye removal – a review. J Environ Manage 90:2313–2342. https://doi.org/10.1016/j.jenvman.2008.11.017

83. Diagboya PN, Olu-Owolabi BI, Adebowale KO (2014) Synthesis of covalently bonded graphene oxide–iron magnetic nanoparticles and the kinetics of mercury removal. RSC Adv 5:2536–2542. https://doi.org/10.1039/C4RA13126F

84. Zhou J, Ma F, Guo H (2020) Adsorption behavior of tetracycline from aqueous solution on ferroferric oxide nanoparticles assisted powdered activated carbon. Chem Eng J 384:123290. https://doi.org/10.1016/J.CEJ.2019.123290

85. Keshvardoostchokami M, Babaei S, Piri F, Zamani A (2017) Nitrate removal from aqueous solutions by ZnO nanoparticles and chitosan-polystyrene–Zn nanocomposite: kinetic, isotherm, batch and fixed-bed studies. Int J Biol Macromol 101:922–930. https://doi.org/10.1016/J.IJBIOMAC.2017.03.162

86. Wu FC, Tseng RL, Juang RS (2009) Characteristics of Elovich equation used for the analysis of adsorption kinetics in dye-chitosan systems. Chem Eng J 150:366–373. https://doi.org/10.1016/J.CEJ.2009.01.014

87. Aharoni C, Tompkins FC (1970) Kinetics of adsorption and desorption and the Elovich equation. Adv Catal 21:1–49. https://doi.org/10.1016/S0360-0564(08)60563-5

88. Sreńscek-Nazzal J, Narkiewicz U, Morawski AW et al (2015) Comparison of optimized isotherm models and error functions for carbon dioxide adsorption on activated carbon. J Chem Eng Data 60:3148–3158. https://doi.org/10.1021/acs.jced.5b00294

89. Yoon SY, Lee CG, Park JA et al (2014) Kinetic, equilibrium and thermodynamic studies for phosphate adsorption to magnetic iron oxide nanoparticles. Chem Eng J 236:341–347. https://doi.org/10.1016/J.CEJ.2013.09.053

90. Razzaz A, Ghorban S, Hosayni L et al (2016) Chitosan nanofibers functionalized by TiO2 nanoparticles for the removal of heavy metal ions. J Taiwan Inst Chem Eng 58:333–343. https://doi.org/10.1016/J.JTICE.2015.06.003

91. Srivastava V, Sharma YC, Sillanpää M (2015) Application of response surface methodology for optimization of Co(II) removal from synthetic wastewater by adsorption on NiO nanoparticles. J Mol Liq 211:613–620. https://doi.org/10.1016/J.MOLLIQ.2015.07.056

92. Dhiman N, Sharma N (2018) Batch adsorption studies on the removal of ciprofloxacin hydrochloride from aqueous solution using ZnO nanoparticles and groundnut (Arachis hypogaea) shell powder: a comparison. Indian Chem Eng 61:67–76. https://doi.org/10.1080/00194506.2018.1424044

93. Hassan N, Shahat A, El-Didamony A et al (2020) Synthesis and characterization of ZnO nanoparticles via zeolitic imidazolate framework-8 and its application for removal of dyes. J Mol Struct 1210:128029. https://doi.org/10.1016/J.MOLSTRUC.2020.128029

94. Choina J, Bagabas A, Fischer C et al (2015) The influence of the textural properties of ZnO nanoparticles on adsorption and photocatalytic remediation of water from pharmaceuticals. Catal Today 241:47–54. https://doi.org/10.1016/J.CATTOD.2014.05.014

95. Dhiman N, Sharma N (2018) Removal of ciprofloxacin hydrochloride from aqueous solution using vertical bed and sequential bed columns. J Environ Chem Eng 6:4391–4398. https://doi.org/10.1016/J.JECE.2018.06.064

96. Alibrahim KA (2023) Adsorption of ibuprofen as a pharmaceutical pollutant from aqueous phase using zinc oxide nanoparticles: green synthesis, batch adsorption, and biological activities. J Mol Recognit 36:e3015. https://doi.org/10.1002/JMR.3015

97. Elhalil A, Farnane M, Machrouhi A et al (2018) Effects of molar ratio and calcination temperature on the adsorption performance of Zn/Al layered double hydroxide nanoparticles in the removal of pharmaceutical pollutants. J Sci: Adv Mater Devices 3:188–195. https://doi.org/10.1016/J.JSAMD.2018.03.005

98. Dhiman N, Sharma N (2019) Removal of pharmaceutical drugs from binary mixtures by use of ZnO nanoparticles: (competitive adsorption of drugs). Environ Technol Innov 15:100392. https://doi.org/10.1016/J.ETI.2019.100392

99. Khoshnamvand N, Ahmadi S, Mostafapour FK (2017) Kinetic and isotherm studies on ciprofloxacin an adsorption using magnesium oxide nanoparticles. J Appl Pharm Sci 7:079–083. https://doi.org/10.7324/JAPS.2017.71112

100. Dehghani MH, Karri RR, Alimohammadi M et al (2020) Insights into endocrine-disrupting bisphenol-A adsorption from pharmaceutical effluent by chitosan immobilized nanoscale zero-valent iron nanoparticles. J Mol Liq 311:113317. https://doi.org/10.1016/j.molliq.2020.113317

101. Agustin MB, Lehtonen M, Kemell M et al (2023) Lignin nanoparticle-decorated nanocellulose cryogels as adsorbents for pharmaceutical pollutants. J Environ Manage 330:117210. https://doi.org/10.1016/j.jenvman.2022.117210

102. Rajendran K, Sen S (2018) Adsorptive removal of carbamazepine using biosynthesized hematite nanoparticles. Environ Nanotechnol Monit Manag 9:122–127. https://doi.org/10.1016/j.enmm.2018.01.001

Publisher's Note Springer Nature remains neutral with regard to jurisdictional claims in published maps and institutional affiliations.